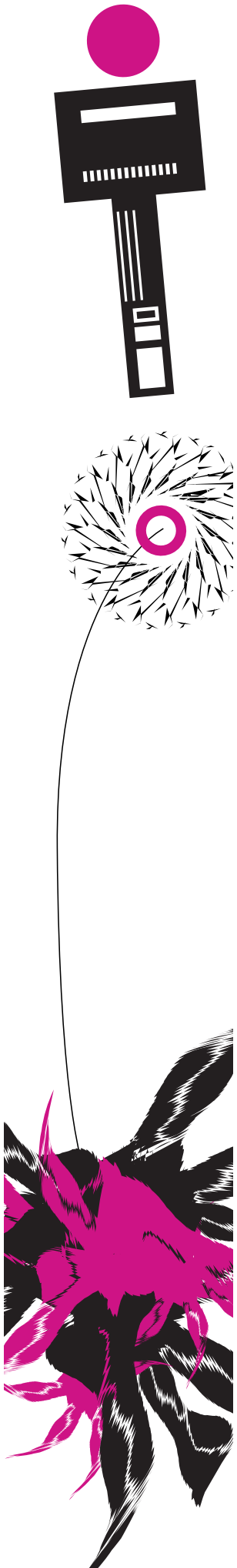

RAM ROBOTICS AND MECHATRONICS

ANTI-BACKLASH MECHANISMS FOR COST-EFFECTIVE CYCLOIDAL DRIVE ROBOTIC ACTUATORS: DESIGN AND EVALUATION

J. (Jelmer) Volbeda

MSC ASSIGNMENT

Committee:
dr. ir. W. Roozing
dr. ir. A.Q.L. Keemink

September, 2024

065RaM2024
Robotics and Mechatronics
EEMCS
University of Twente
P.O. Box 217
7500 AE Enschede
The Netherlands

UNIVERSITY OF TWENTE. | TECHMED CENTRE

UNIVERSITY OF TWENTE. | DIGITAL SOCIETY INSTITUTE

Anti-Backlash Mechanisms for Cost-Effective Cycloidal Drive Robotic Actuators: Design and Evaluation

Jelmer Volbeda (s2865629)
Robotics & Mechatronics (RaM) Group
MSc Robotics - University of Twente

***Abstract*—3D-printing is a promising method for cost-effective actuator designs, but it often results in less precise tolerances, leading to increased play. In this work, we propose two novel anti-backlash mechanisms for cycloidal reducers. One uses a conically shaped cycloidal disk, and the other uses a split non-pinwheel design. Both were integrated into a compact actuator design. Two prototypes were manufactured and extensively tested in comparison to a baseline model. Experimental results show that the proposed mechanisms reduce play at the cost of increased friction. Both mechanisms utilize an adjustable preload that can be configured for the intended application based on the trade-off between play and friction. Furthermore, the designed actuator demonstrates performance that is competitive with recent works. Using 3D-printed components proves to be a viable manufacturing method for cost-efficient designs.**

***Index Terms*—Cycloidal Drives, Robotic Actuator, QDD, Anti-Backlash, 3D-printing, Legged Robots**

I. Introduction

Interest in legged robotics, like quadrupeds and humanoids, has grown recently. These robots require power-dense actuators like the popular open-source designs of the MIT cheetah quadruped [1] or the ARTEMIS humanoid robot [2]. These robots use so-called quasi-direct drives (QDD), which feature high actuator transparency [3]–[8]. This allows for torque control, shock absorption, and highly dynamic motions.

Actuators are often a large part of the cost of a robot. The use of 3D-printed components enables a cost-effective design approach while allowing for easier customization of parts to meet the specific design and requirements of the robot. However, 3D-printing does come with inferior material properties and looser machining tolerances compared to the traditional method of machining metal parts. Most actuator designs use planetary gears. These reducers have small feature sizes that require tight tolerances. Furthermore, the torque transmission relies on the shear strength of the teeth. Cycloidal reducers are an improvement in both aspects, as they have larger features for similar reduction ratios and sizes, and they rely solely on compressive forces. Cycloidal reducers are therefore more suitable for 3D-printing. These reducers are also particularly resistant to shock loads, which legged robots frequently experience. This makes cycloidal drives an interesting choice for a 3D-printable QDD actuator. This idea was explored in [3], [4] with promising results.

Transmission transparency is essential for QDD actuators, requiring minimization of non-linear effects like backlash, friction, and transmission error. Prior work shows good performance even with play in the reduction stages. However, reducing play further can simplify and improve control methods. Especially in humanoid robots where play accumulates across joints. 3D-printing has less precise tolerances than traditional machining, requiring more clearance, resulting in increased transmission backlash. A mechanical solution is to use an anti-backlash mechanism with preloading. Preloading of spur gears is a well-established method [9]. A similar strategy is possible with other reducer types, such as cycloidal drives.

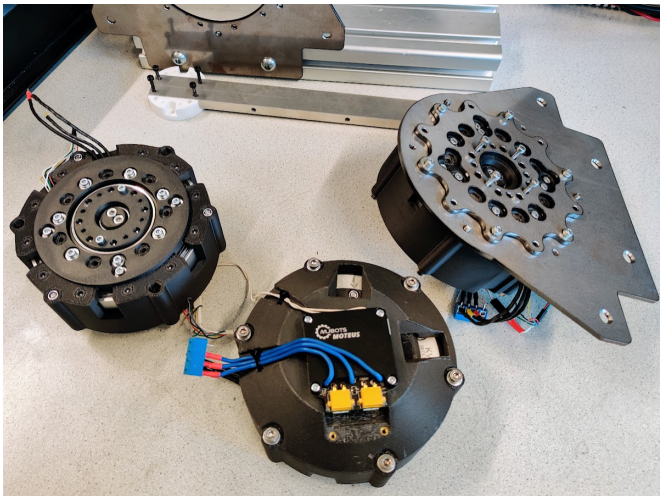

Fig. 1: Three prototypes of the proposed actuator design.

The goal of this research is to develop a compact, cost-effective, and high-power actuator for legged robots with minimal play. Two anti-backlash mechanisms are developed and integrated into the design of a cycloidal reducer QDD actuator, and their performance is tested. Custom parts are manufactured using additive manufacturing, specifically fused deposition modeling (FDM) 3D-printing. The main contributions of this paper are as follows:

1) A cost-effective QDD actuator with a non-pinwheel cycloidal reducer, offering performance comparable to recent designs and built from mostly 3D-printed and off-the-shelf components.
2) Two novel anti-backlash methods for cycloidal reducers using a preloading mechanism, incorporated into variations of the designed actuator.
3) Experimental validation of the effect of preload in both anti-backlash mechanisms against a baseline design.

TABLE I: Specification of various QDD actuators. (*Estimated values.)

	Proposed design	**Roozing et al. [3], [4]**	**Lee et al. [5]**	**Singh et al. [6]**	**PULSE 115-60 [7]**	**Yu et al. [8]**	**MIT Cheetah [1]**	**ARTEMIS hip pitch [2]**	**ARTEMIS hip yaw [2]**	**Unitree GO M8010-6 [10]**	**Unitree M107 [11]**
Intended application	Humanoid	Legged robots	Legged robots	Quadruped	Dynamic QDD	Hip Exo-skeleton	Quadruped	Humanoid	Humanoid	Quadruped	Humanoid
speed [RPM]	120 (45V)	367 (40V)	177 (80V)	255 (48V)	90 (48V)	188 (42V)	382 (24V)	220 (44V)	239 (44V)	286 (24V)	unknown
nominal torque [Nm]	52 (20A)	36.4 (40A)	unknown	26.4	18.5 (14A)	17.5 (7.5A)	6.9	80	30	unknown	unknown
peak torque [Nm]	156 (62A)	unknown	150 (40A)	55.2	62.5 (3.6A)	42 (17A)	17	250	85	23.7 (40A)	360
diameter [mm]	125	104	90	126	113.8	110	96	200*	100*	96	107
height [mm]	62	58	37	68	64.2	51	40	60*	80*	42	74
mass [kg]	1.35	0.797	1.85	1.89	1.25	0.77	0.48	3	0.815	0.53	1.9
Peak torque density [Nm/kg]	115.6	45.7	81.1	29.2	50.0	54.5	35.4	83.3	104.3	44.7	189.5
Power density [W/kg]	1452.2	1755.3	1502.9	780.0	471.3	1073.9	1416.8	1920.0	2610.4	1339.3	-
Reducer type	Cycloidal	Cycloidal	Cycloidal	Planetary	Planetary	Planetary	Planetary	Planetary	Planetary	unknown	unknown
Reduction ratio	13	11	11	8	5	8	9	5.9	14.5	6.3	unknown

The next sections are outlined as follows: Sec. II describes the design requirements and details prior work and relevant literature. Sec. III describes the proposed design regarding actuator assembly, implemented anti-backlash mechanisms and their working principles, and constructed prototypes. Sec. IV describes the test setup, data processing methods, and results. The final sections provide discussion and conclusions.

II. Background and Requirements

A. Design requirements

Several requirements are set for the designed actuator. For this, other QDD actuators are taken as references to define viable size, torque, and speed requirements. Table I lists specifications for a variety of QDD actuator designs. The specifications of the proposed design are included as well. Most of the included actuators are intended for quadruped robots. Humanoids do require actuators with higher torque capacities. Therefore, bio-mechanics data of human legs is taken as an additional reference. [12] shows knee, hip, and ankle torques and velocities during jumping and sprinting. Peak values while jumping are around 4 Nm/kg torque and speeds of 130 RPM. [7] takes a similar strategy based on measurements of inclined walking ([13]) and defines comparable requirements.

Based on that, the following requirements were set:

- It must be of suitable torque and speed for the hip or knee of a humanoid robot. That is 40 Nm nominal torque, 100 Nm peak torque, and a peak velocity of 130 RPM.
- It must be of competitive performance relative to recent works (shown in Table I). This includes a size less than 130 mm by 65 mm, and a mass below 1.5 kg.
- It must integrate an anti-backlash mechanism.
- It should be cost-effective by prioritizing custom 3D-printed parts alongside off-the-shelf components.

B. Reducer types

To provide a good understanding of cycloidal reducers, it is useful to contrast them with other common reducer types. Fig. 2 shows typical ratio ranges for various reducer types (adapted from [5]). These ranges are not strict limits but represent typical values, beyond which issues such as transmission error, torque wobble, and increased geometric complexity become more significant. A brief description of the most relevant types follows.

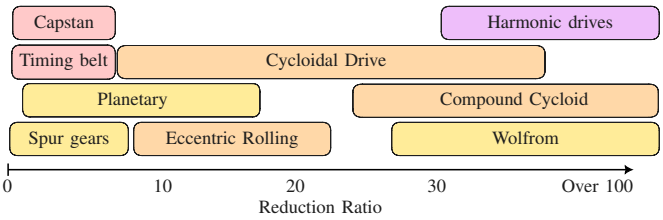

Fig. 2: Typical transmission ratios for various reducer types.

Spur gears, *timing belts*, and *capstan drives* only offer relatively low reduction ratios due to their direct gear or cable-based mechanisms. They are simple in construction and efficient for low transmission ratios. However, achieving high reductions requires multiple stages, which increases system complexity and can reduce overall efficiency.

Planetary gears provide a compact and efficient solution for slightly higher reduction ratios. They are the most commonly used type of reducer in QDD drives, as shown in Table I. The internal gear arrangement of planetary gears allows multiple teeth to engage simultaneously, increasing torque capacity. Multiple stages, or variations like *Wolfrom drives*, can extend the range of reduction ratios but increase complexity [17].

Cycloidal reducers offer a unique combination of high torque capacity, high stiffness, low backlash, and back-drivability. This comes from a mechanism with rolling contact

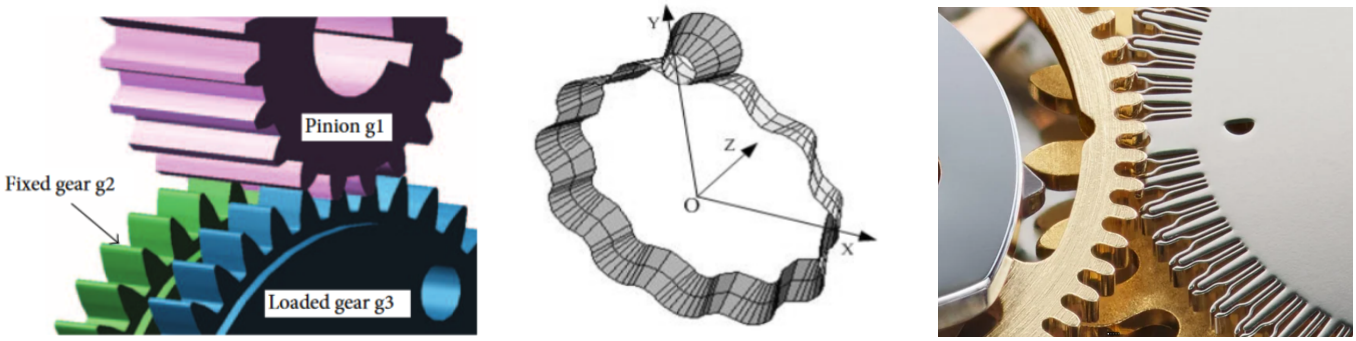

(a) Split gears [14]. (b) Conic cycloidal gear [15]. (c) Spring teeth [16].

Fig. 3: Three types of anti-backlash mechanism.

of multiple teeth simultaneously. The cycloidal profile is derived from epitrochoid equations, representing the path traced by a point on a circle rolling around a larger circle. This shape is determined by the pitch circle (R), radius (R_r), and amount (N) of rollers on the pinwheel, along with the eccentricity of the disk's motion (E). These parameters are indicated in Fig. 4 (adapted from [3]). More information on the working principles, construction, and optimization of cycloidal drives is given in [18], [19].

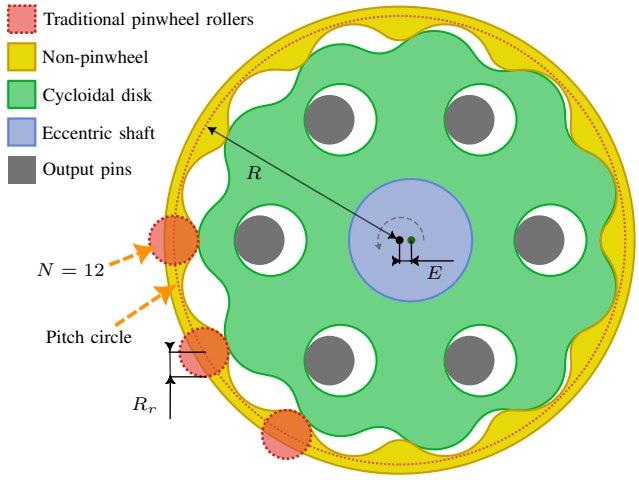

Fig. 4: Diagram of a cycloidal disk and non-pinwheel design.

A more recent trend is the use of ideal non-pinwheel profiles for even larger tooth contact and reduced complexity [20]. A non-pinwheel design is included in Fig. 4. Cycloidal drives cover a wide range of reduction ratios, making them versatile for various applications. *Compound cycloidal* and Rotate-Vector configurations can further extend this range. *Eccentric rolling* transmissions offer a simplified alternative by using a single input gear to engage with an outer cycloidal profile [21].

Harmonic drives are known for high precision and low backlash at higher reduction ratios. Harmonic drives use a flexible inner gear that meshes with a rigid outer gear. The input drives an elliptical wave generator that deforms the flexible gear. While popular within robotics and suitable for certain applications, they generally have lower efficiency and limited backdrivability. This makes them less ideal for QDD systems, compared to cycloidal reducers [22].

C. Anti-backlash mechanisms

A common problem with transmissions for high-precision applications is play or backlash. This is an unwanted gap between gears. The result is free motion at the output even when the input is fixed. This also appears as a slight delay when changing direction. This gap can be caused by wear or under-dimensioned parts. Some under-dimensioning is always required for assembly. This makes backlash unavoidable with standard transmissions. Non-linear control methods do exist that can maintain accurate performance, even in systems that experience backlash [23]. However, this comes with limitations and additional control complexity. Mechanical solutions also exist. These are mainly used with spur gear transmissions. Similar principles can be applied to other reducer types, but the available literature on this is limited. Several relevant principles are described in the following.

1) Split gears: The most common method of countering play in spur-gear transmission is with the use of a split gear. This can be implemented in various ways [9]. In most cases, two spur gears are stacked. One gear is rigidly coupled to the shaft, while the other is attached to a torsion spring with some phase offset. Fig. 3a shows this in a model. When meshing, the gears are forced together. The torsion spring ensures both sides of the gear teeth are always in contact. The split gear method does come with a more complex gear meshing. Ideally, the loads should not exceed the preload force [24].

The main principle of this method is that there are parallel power transmissions from the individual gears. A novel anti-backlash mechanism for Wolfram-type reducers shown in [17] similarly relies on this principle. Cycloidal reducers often use two disks for balancing, in which case the same principle method can be applied.

An implementation of the split gear method applied to a cycloidal drive is seen in [25]. It shows a method of implementing the concept into a cycloidal reducer design but features no quantitative results.

2) Conic-shaped gears: Another method is to use conically shaped gears. The pitch diameter increases along the width of a gear. By offsetting the gear axially, the effective distance in meshing lines is adjusted. This method has been applied to cycloidal transmissions before. [15] shows an example of using conic-shaped pins to counter backlash. The rollers of the pinwheel are conic-shaped and the meshing equations are adjusted accordingly. Fig. 3b shows the created disk profile and a conic roller. Another implementation is found in [26], featuring an RV-reducer design with a similar beveloid cycloidal disk profile. Both feature theoretical and experimental results that confirm a reduction in backlash.

3) Spring-shaped gear teeth: Another method of countering undersized gear teeth is by integrating springs into each tooth of the gear. This idea is seen in some patents for timepieces [27], [28]. An implementation can be seen in the Rolex 4130 mechanical watch, where each gear tooth consists of two leaf springs. This is shown in Fig. 3c. The gear teeth are slightly oversized to create a preload.

A similar approach could be applied to cycloidal reducers. By preloading the pins of the outer ring radially while constraining them tangentially, compensation for an undersized disk could be achieved. Alternatively, incorporating a flexure element into the disk could provide the necessary preload.

D. QDD design

Key features of prior QDD designs are outlined in the following. These elements served as inspiration for the design of the proposed actuator.

1) Motor-embedded reduction: Recent work on high torque density actuators for humanoid robots is the ARTEMIS robot [2]. These actuators provide relatively high torques to enable highly dynamic motions. It uses a series of custom QDD actuators. The largest configurations offer 80 Nm and 250 Nm peak torques, and 240 RPM and 220 RPM max speeds, respectively. The packaging of these actuators is similar to those of the MIT Cheetah [1], a well-known quadruped design. It uses an outrunner motor with a large air gap radius and motor-embedded gearing. The large radius actuator provides high torque, and a low reduction ratio ensures low reflected inertia. Outrunner motors feature high torques and a hollow cylindrical shape. Compact and torque-dense packaging can be achieved by embedding the reduction stage into the empty center of this. [2] features a chart of torque density for various actuators that highlights the relatively high torque density of the actuators for the MIT Cheetah and ARTEMIS robots.

2) Non-pinwheel designs: The common cycloidal drive consists of a disk with a cycloidal profile and a pinwheel of equally spaced circular rollers. These rollers are often free to rotate on bearings. An alternative is to use an internal cycloidal profile to replace the pinwheel. This profile matches the ideal meshing profile and ensures larger tooth contact. This provides an output with lower vibrations and even higher shock resistance [20]. This method also greatly reduces part count and complexity. Non-pinwheel designs are also ideal for 3D-printing as the whole pinwheel is reduced to a single, easily manufacturable part. In [3] an experimental comparison was done between two 3D-printed cycloidal reducers. One with freely rotating (bearing-supported) rollers, and one with the ideal non-pinwheel profile. The results show only minimal differences in performance between the two reducers. This means a non-pinwheel design can provide similar performance with a significantly reduced complexity.

3) High torque capability: Another useful design aspect is found in the compact cycloidal reducer from [5]. This is a complete actuator package focused on high torque output. It features details on the needed stiffness of the housing to support these torques. A stiffening frame is used to support the output pins from both sides to increase the output stiffness. Sub-carriers that are separate from the output pins are implemented to provide additional rigidity to the combined output structure.

III. Implementation

A. Actuator Design

The proposed QDD actuator is designed to achieve a compact, high-torque, easily manufacturable, and low-cost package. All while maintaining competitive performance to recent, more traditional actuator designs. Cross-sections of the CAD design are shown in Fig. 5. All relevant files to recreate or modify the design are provided at [29]. The design is largely parametric and therefore relatively straightforward to modify to account for alternative reduction ratios.

The selected motor is the frameless RO100 from CubeMars, which has a high torque capability and a large hollow shaft. The largest frameless motor of the series is selected to leave more space for the integration of the reducer and anti-backlash mechanisms. This is an off-the-shelf part which is in contrast to many earlier designs. For example, the ARTEMIS actuators use custom wound motors [2]. The frameless motor forms the foundation for the rest of the actuator design.

To complete the design, a Moteus r4.11 motor controller was selected. This is a low-cost driver that comes with an onboard encoder. The motor driver is positioned on the housing cap such that the magnetic encoder is centered above the input shaft.

The actuator incorporates motor-embedded gearing, a non-pinwheel cycloidal reducer, and a single disk configuration with a reinforced output structure. These design elements are described in detail in the following.

1) Motor-embedded reduction: As described in section II-D1, a compact package can be achieved by positioning the reduction stage at the center of a large radius frameless motor. The same packaging is used in the proposed design. A reduction ratio of 13:1 is selected to match the torque and speed requirements with the selected motor. This ratio is relatively high for QDD actuators but was chosen to get a higher maximum torque. This is done because the torque limits of the 3D-printed component will be most interesting to test, as opposed to higher speeds. The use of a frameless motor means that the corresponding bearings need to be integrated into the

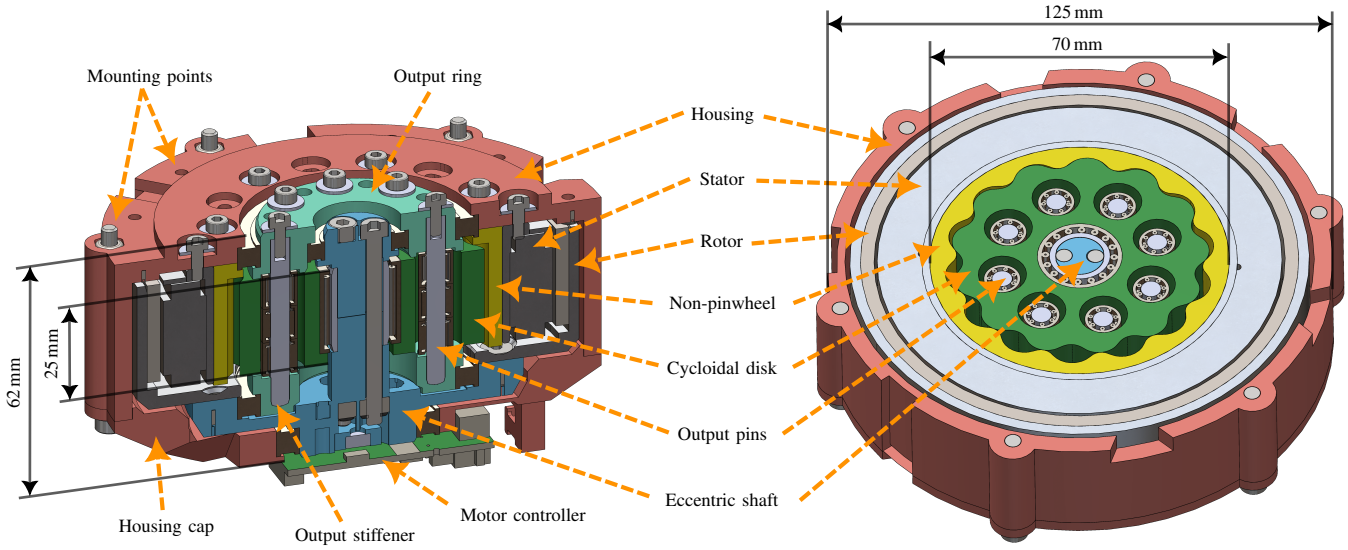

Fig. 5: CAD cross-section of the baseline design.

actuator package. The proposed actuator is only slightly larger than the structure required to integrate such a motor.

2) Non-pinwheel cycloid gearing designs: The proposed design features a non-pinwheel design, inspired by the designs mentioned in II-D2. This allows the non-pinwheel to be smaller in diameter as it does not need to house fully round roller pins. The parameters used are shown in Table II.

TABLE II: Cycloidal profile parameters.

N	14	Pinwheel roller number
R	34 mm	Pitch circle radius
R_r	3.5 mm	Pinwheel roller radius
E	1.5 mm	Disk eccentricity

This non-pinwheel part is centered in the stator of the frameless motor, which provides good support against deflection. Because of this, the cycloidal profile can be of a larger radius which helps to resist higher torques. The single-part design of this non-pinwheel also allows for a more straightforward implementation of the anti-backlash mechanisms.

3) Single disk with counterbalance: The eccentric motion of a cycloidal drive and the off-center disk inherently come with vibrations. Most designs solve this by having two disks with opposite phases, balancing out any vibrations in the plane of motion. However, this also increases the complexity of the design. Additionally, it adds over-constraint within the structure. When combined with manufacturing inaccuracies, this can result in internal stresses.

An alternative is to use a single disk in combination with a counterbalance. This method is also used in the RIC arm prosthetic which features a specially compact cycloidal reduction stage [30]. This is combined with a fixed roller pinwheel design. With the designed actuator, the same decision is made. Only one cycloidal disk is used. A counterbalance is integrated into the supporting part for the rotor of the frameless motor. The use of a single disk greatly reduces the complexity of the design, which also aids the implementation of the anti-backlash mechanisms.

4) Stiffening frame on output pins: The double supports for the output pins, as described in Section II-D3, are also integrated into the proposed design. The output pins are rigidly attached on either side. Separate sub-carriers (as in [5]) are omitted to maximize the number of output pins. The design includes eight output pins, each fitted with three drawn-cup needle bearings. This combined output structure is supported by a double-bearing arrangement such that the output can also take off-axis loads.

5) Output mounting methods: The output structure has eight output pins of hardened steel with internal M3 threads. These threads are exposed to the outside and can be used to mount an output. This ensures the output is rigidly tied to the larger output structure and not exclusively reliant on a 3D-printed component.

In addition, the output ring has eight embedded M4 locknuts that can also be used to mount the output. The use of locknuts with nylon inserts helps prevent screws from loosening due to vibrations. Therefore it is ideal to mount the output using a combination of both the locknuts and output pins.

6) Reinforcing screws: The design mainly consists of 3D-printed components. The housing consists of a large cup-shaped piece with a cap piece. The cap piece gets attached with screws that pass through to the other side of the housing. This reinforces the thin walls, especially so in the weakest direction, which is layer-to-layer adhesion. These same screws can also be used to attach the actuator to another structure ensuring optimal rigidity at the mounting interface.

The eccentric shaft is the thinnest load-bearing part and is therefore expected to be a weak point of the design. Therefore, this part is also reinforced by long screws that pass through its full length. Additionally, a shaft liner is incorporated into this

part to provide a hardened steel raceway for the corresponding bearing. The liner fits tightly on the eccentric shaft, providing additional rigidity. The eccentric shaft piece is split in the middle to allow for assembly and the mentioned bolts fix this in place.

Embedded locknuts are used in several locations for the reinforcement screws but also for the fastening hardware. These are to further prevent the screws from vibrating loose.

B. Anti-backlash mechanisms

The design shown in Fig. 5 uses a traditional cycloidal reduction. This design is used as a baseline for experimental comparison. Two of the researched anti-backlash principles were integrated into separate variations of this actuator design. These are referred to as the conic disk design and the split-pinwheel design. The design of the actuator as a whole is optimized to allow changing between configurations with minimal modified parts. This is to enable a fair comparison of the different mechanisms.

1) Conic disk: The profile of the cycloidal disk is defined by several parameters, among which is the radius of the rollers on the pinwheel. The conic cycloidal disk is generated by assuming conic rollers on the pinwheel. This means the pinwheel roller radius is increasing along the axial direction. Several cycloidal profiles are generated with a linearly increasing pinwheel roller radius.[1] The resulting profiles are connected using a lofting feature within the CAD software. The non-pinwheel profile is derived from the disk profile. Therefore the conic non-pinwheel is generated using the same methodology. The resulting reducer parts have a clearance that depends on their axial offset. Fig. 6 shows the relevant components, including the adjustment mechanism. The cylindrical design fits efficiently withing the motor-embedded design.

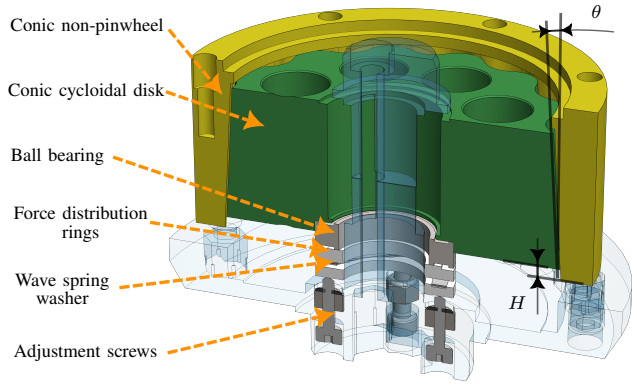

Fig. 6: Modified parts for the conic disk design.

Adjustment screws that push against the conic disk are added within the eccentric shaft. As these parts are rotating relative to each other, a bearing is added in between. Additionally, a spring is added. This causes the adjustment to be more of a preloading force as opposed to a fixed setting. It allows more movement and compensation within the anti-backlash mechanism. As long as the spring remains under compression, the mechanism will automatically compensate for some wear of the reducer parts. The use of a preload is also expected to compensate better for play that varies throughout a rotation of either the input or the output.

The disk and pinwheel are conic with an angle of $\theta = 3.5$ degrees and have an adjustment range of $H = 3$ mm. This creates a maximum adjustment equal to 0.16 mm radially, which corresponds to a uniform offset or clearance. The selected preload springs are wave spring washers. Two are stacked to increase the preload force, each providing 27 N at maximum compression.

2) Split pinwheel: This anti-backlash mechanism relies on the split-gear method of preloading. The pinwheel is split into two stacked rings with the non-pinwheel cycloidal profile. A slight relative rotation between either ring causes an offset of the two non-pinwheel profiles. This causes an effective widening of the pinwheel lobes. This will take up any clearance between the disk and the pinwheel. Fig. 7 shows the relevant components of this mechanism.

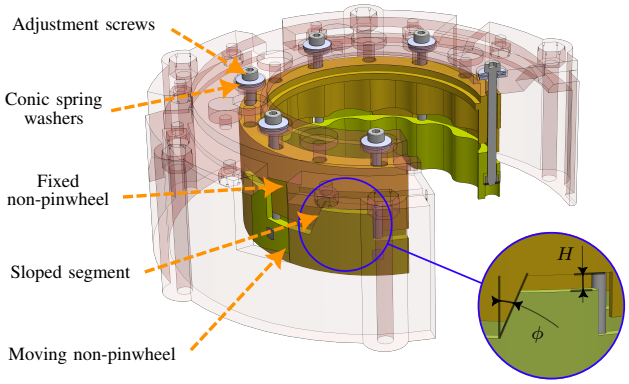

Fig. 7: Modified parts for the Split-pinwheel design.

This relative rotation of the two rings must be adjustable with a mechanism that fits within the cylindrical package of the motor-embedded reducer design. This is done by adding sloped segments around the split of the rings. These segments cause a screw-like motion when the two rings are clamped together. This clamping force is created by several bolts that are accessible from the top of the actuator housing. Conic washers are added at these bolts to create a limited stiffness. Same as with the conic design, this makes it easier to adjust the preload and creates a buffer to compensate for wear over time.

The axial adjustment range is again $H = 3$ mm. The sloped segments have an angle of $\phi = 114$ degrees (shown in Fig. 7), resulting in a maximal adjustment of $\alpha = 2$ degrees relative offset between the pinwheels (as shown in Fig. 8. The anti-backlash mechanism has the most effect on the edges of the non-pinwheel lobes as these are the main contact points [31]. The radius at these points is $r_c = 31$ mm. This means

[1]The cycloidal disk and non-pinwheel profile generation was automated using Python scripts that export the profiles to a DXF. These scripts are available at [29].

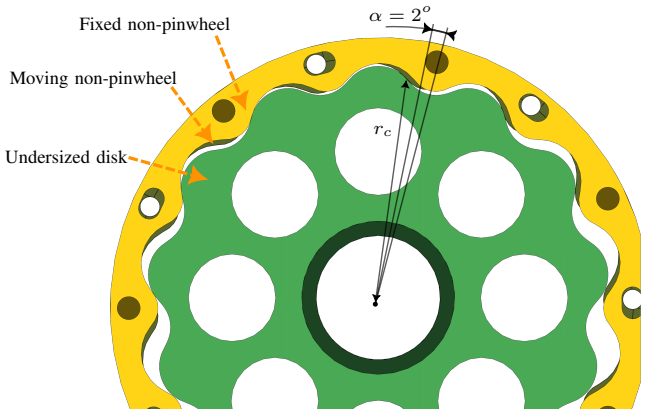

Fig. 8: Isometric top view of split pinwheel design showing meshing with an undersized disk.

the 2 degrees rotation has a maximal adjustment of around $r_c tan(\alpha) = 1.1$ mm near the lobes. At this configuration, the pinwheels compensate for a disk that is undersized by 0.37mm. This configuration with an undersized disk is shown in Fig. 8.

The split pinwheel design uses conic washers on each of the seven adjustment screws. Four are stacked to increase the compression range. These springs each provide 79 N when halfway compressed. The total preload force achievable by this is higher then that of the conic disk design. However the split pinwheel has several parts adding friction. The conic disk mechanism is less constrained so the adjustment requires less force.

C. Prototypes

Several custom parts were required in addition to the off-the-shelf components. These custom parts were 3D-printed in PC-CF (Prusament Polycarbonate with Blend Carbon Fiber), a material that is exceptionally rigid and ideal for structural components. However, it is unsuitable for wearing parts such as the cycloidal disk and pinwheel, so these were printed in an alternative material. PA6-CF (MarkForged Onyx) was chosen, as nylon is wear-resistant and the carbon fiber improves rigidity. [2] The printed components and several bearings are shown in Fig. 9. The assembled actuators are shown in Fig. 1.

The PC-CF parts were printed on a Bambu Labs X1 carbon with print settings configured as 4 wall lines, 37% infill, and layer heights of 0.2mm. The Onyx parts were printed on a MarkForged printer using 2 wall lines, 37% infill, and 0.2mm layer height.

The seams of the 3D-printed parts impacted the motion of the reducer parts. The largest impact results from seams within the output holes of the cycloidal disk. To address this, the holes were printed slightly undersized (by 0.1 mm) and then reamed to the correct dimension.

The total weight of the assembled actuator is 1.350 Kg of which 0.3 Kg is printed components. The total cost of the designed actuator is around $327, as detailed in Table III. The variations including an anti-backlash mechanism cost around $7 more as they require additional springs and hardware.

[2]Reducer parts of PC-CF were initially tested but resulted in excessive wear. A PC-PA (Taulman Alloy 910) material was also tested but this material showed a significant drop in stiffness at increasing temperatures.

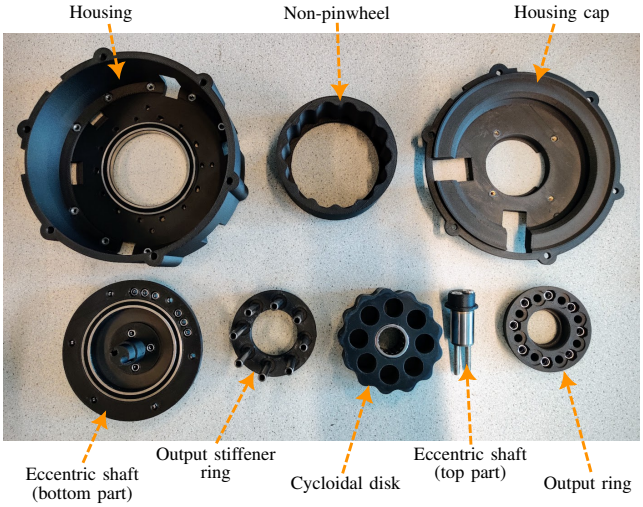

Fig. 9: 3D-printed components of the actuator.

TABLE III: Materials and costs

Frameless motor (RO100)	$171
Motor controller (Moteus r4.11)	$79
Bearings	$47
Hardware	∼$10
3D-printing filament	∼$20
Total	∼$327

IV. Results

A. test setup

During the tests, the actuators are controlled from the moteus python interface which communicates through a USB to CAN-FD device (fdcanusb by mjbots [32]). Several scripts were written to largely automate the test process. These scripts are released in [29]. For the tests, the actuators are rigidly mounted used steel mounting plates manufactured from 3 mm sheet. This setup is shown in Fig. 13.

B. Anti-backlash mechanism performance

For the friction test, the actuator is mounted without anything on the output. This means it is free to rotate, except for any internal frictions and resistances. The actuator is controlled to slowly increase in speed. This is done using the internal trajectory planner of the motor controller which is set to a corresponding acceleration limit. The speed ramps up to a specified maximum and then ramps back down. The test is repeated in the opposite direction. Data is continuously recorded throughout the motion at the maximum achievable rate. This ranged between 100 Hz and 400 Hz depending on the number of monitored variables. Among the collected data are the current speed and torque. This info is used to estimate a friction model.

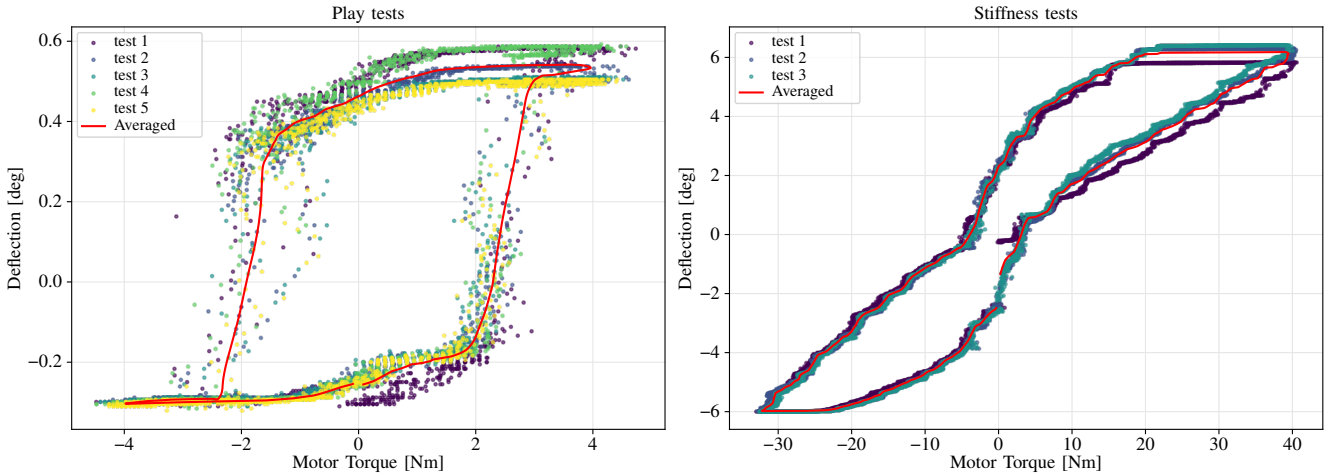

Fig. 10: Data processing to average multiple torque ramp repetitions.

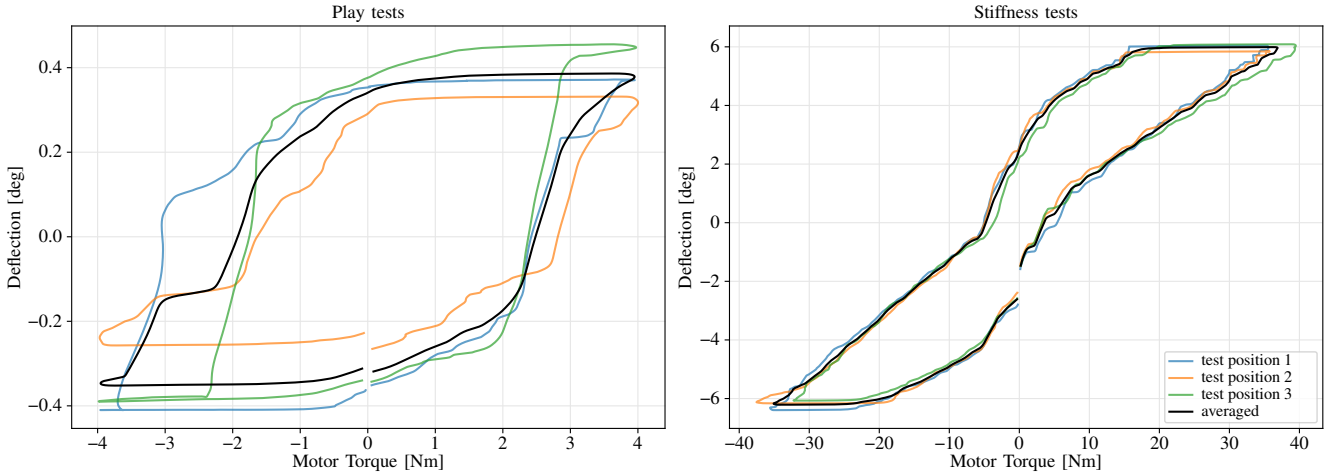

Fig. 11: Data processing to average the results for various locked orientations.

The reducer play and stiffness are estimated from another test. This is tested with a locked output. A steel locking plate was manufactured that fixes the output to the mounting plate. This setup is shown in Fig. 13. As the output is fixed, any possible motion of the input will be a combination of play and limited stiffness. With this fixed output, the actuator is commanded to do a slowly ramped torque up to a specified value and back down. It then repeats in the opposite direction. This is repeated multiple times to get more data points and more reliable measurements. A low torque is used for the play estimates and a larger torque is used for the stiffness estimates. An important thing to note here is that these recordings are done at the input and then scaled by the reduction factor. These results might therefore be slightly different than what would be measured at the output. The relevant metric depends on the intended application.

1) Data processing methods: To get more accurate results for the play and stiffness tests. These torque ramps are repeated multiple times and then averaged. This is done by interpolating each torque versus deflection curve to the same amount of data points, followed by some filtering to remove noise. Then for each point along the curve an average of all test repetitions is taken. The recorded points and averaged curves for the play and stiffness tests are shown in Fig. 10.

The play and stiffness are also expected to be dependent on the orientation of the output. To compensate for this effect, the tests are repeated at three different locked positions. The resulting curves from these tests are combined using the same processing steps as used for the multiple ramp repetitions. The intermediate results and averaged curve are shown in Fig. 11.

The resulting curve of torque versus deflection is the average of several torque ramp repetitions at multiple locking positions. This final curve is used to estimate play and stiffness. Reducer play is estimated as the deflection difference at zero torque when approached from opposite sides. The stiffness is estimated from the slope of the deflection during an increasing

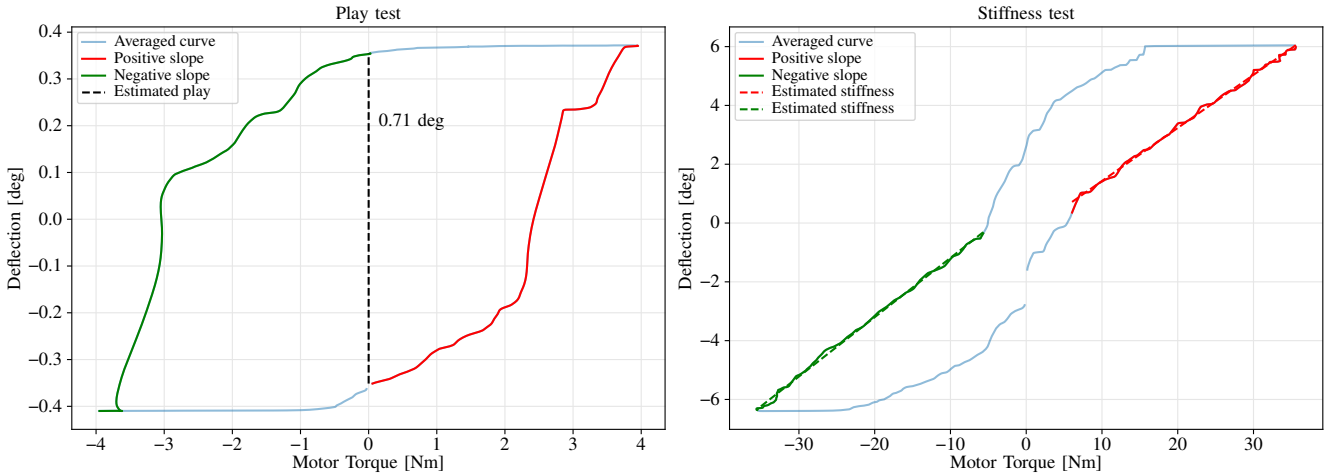

Fig. 12: Data processing to estimate play and stiffness from torque versus deflection curves.

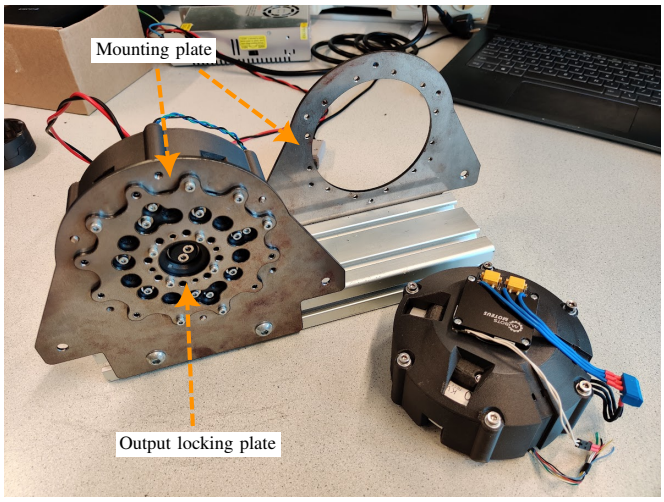

Fig. 13: Actuator mounting plate and output locking plate for torque tests.

torque, ignoring the initial part affected by the play. The estimated value for play is used for this. An example of the estimated play and fitted stiffness lines is shown in Fig. 12.

2) Run-in: The friction, play, and stiffness for each actuator were tested after the initial assembly. Following this, the actuators were run at a constant speed in alternating directions for 90 minutes. This is the run-in period and serves to wear in any high spots in the reduction stage and get to a repeatable state. Throughout the tests, it was noticeable that the torque to overcome internal frictions reduced over time until it reached a constant value. This test also provided some insights in the thermal performance of the actuators. Temperature seems to rise relatively quickly and therefore the maximum speed during the run-in tests had to be limited. At the run-in speed of 21 RPM, the temperature stopped rising around 55 °C.

3) Effect of preload adjustment: After the run-in period, the tests of friction, play, and stiffness were repeated again. Next, the anti-backlash mechanisms were tested. This is done by repeating all tests after incremental increases in the preload. For each step, the preloading screws were adjusted an equal amount. Incremental adjustments were made until the amount of play stopped decreasing. The averaged torque versus deflection curves of each actuator and test moment are shown in Figs. 15, 16 and 17. These include the results before and after run-in, and at each preload increment.

The play and stiffness were estimated from the averaged torque versus deflection curves of each test moment. Additionally, at each test moment, a speed ramp was recorded. These are used to estimate the friction at each preload increment. The resulting values are all shown in Fig. 14. This shows how the performance changes as a result of run-in and preload increments.

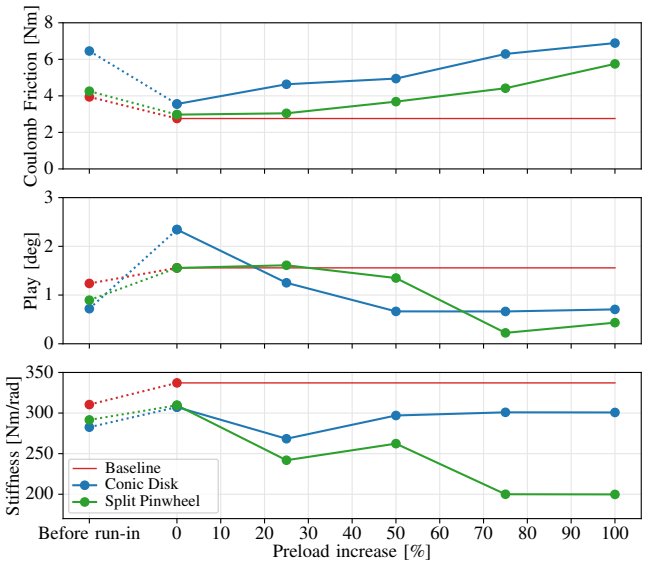

Fig. 14: Effect of preload on friction, play, and stiffness.

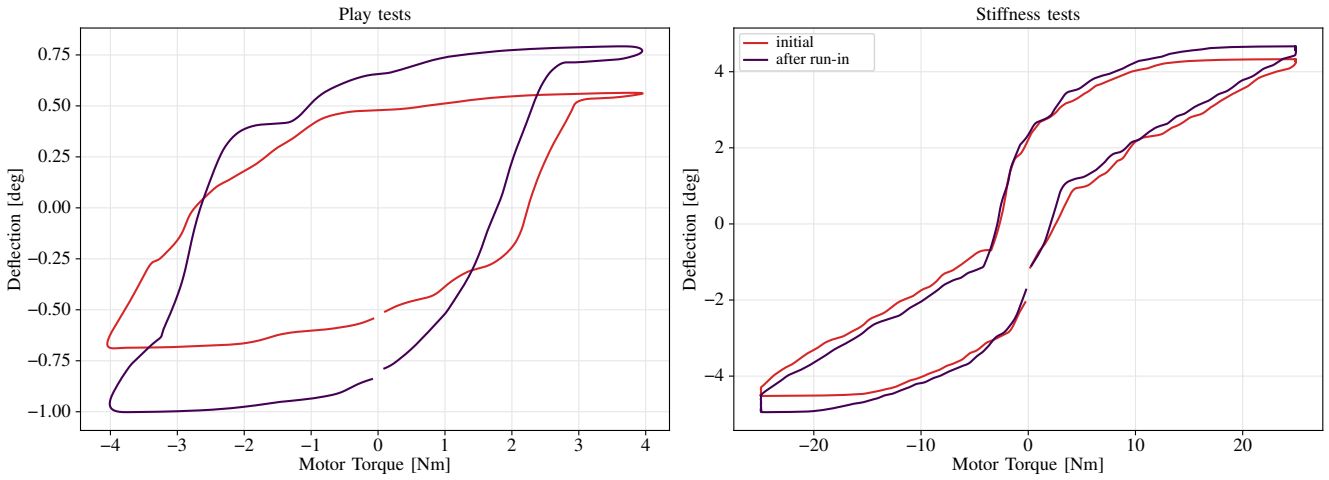

Fig. 15: Torque versus deflection curves for the baseline design.

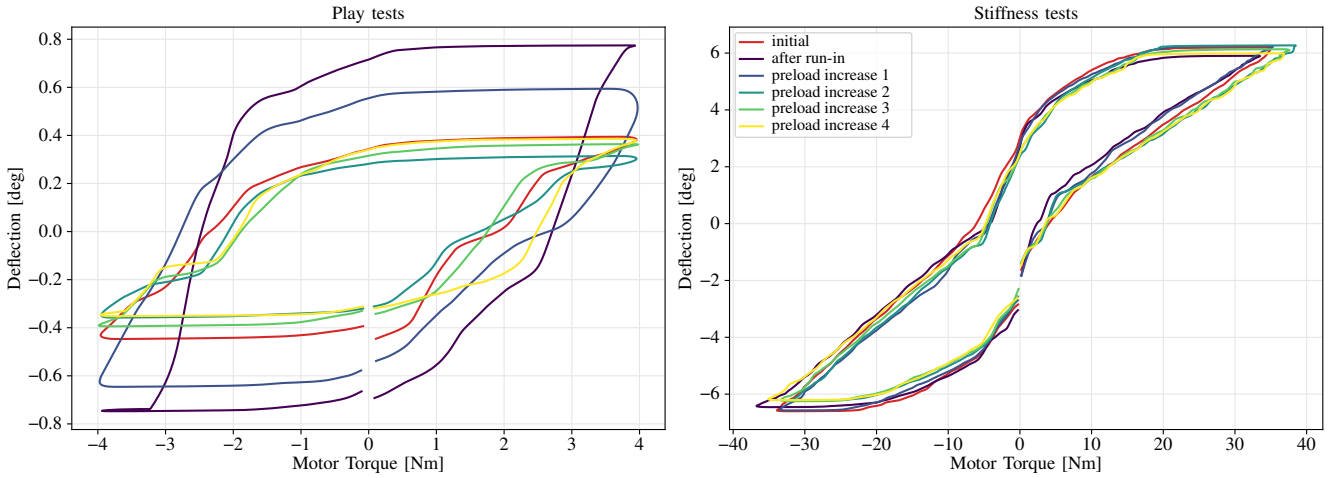

Fig. 16: Torque versus deflection curves for the conic disk design.

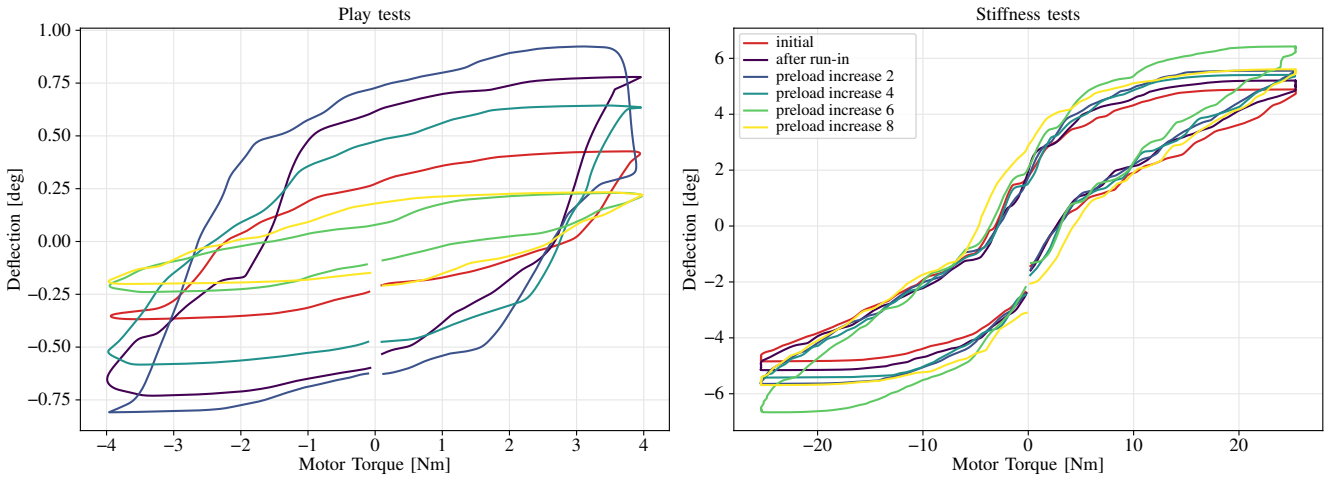

Fig. 17: Torque versus deflection curves for the split-pinwheel design.

The primary trade-off for determining the correct preload, is the reduction of play at the expense of increased friction. This trade-off is better illustrated by the Pareto front shown in Fig. 18. Each datapoint represents a tested preload settings, with the baseline added as a single data point. Ideally, friction and play are both minimized. Therefore points closer to the origin indicate better performance.

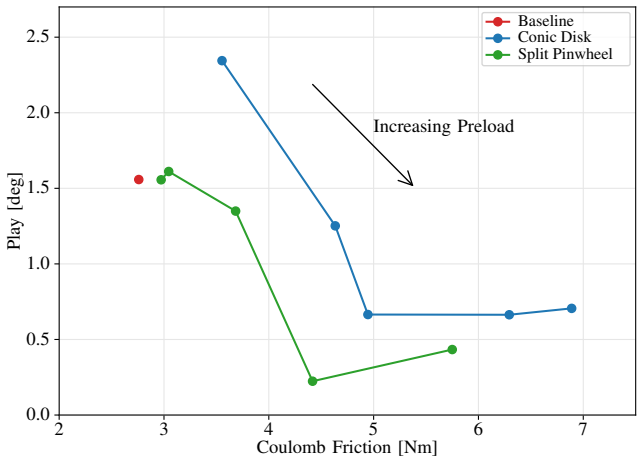

Fig. 18: Tradeoff between play and friction.

C. Actuator performance

The constructed actuator was tested to validate its performance and to test the strength of 3D-printed components and cycloidal drives in torque-dense actuators. These tests were done using the baseline actuator.

1) Maximum Velocity: The maximum speed of the actuator was tested without anything on the output. The actuator is commanded to move at a slowly increasing speed until the speed reaches its maximum and can no longer keep up with the commanded speed.

With a supply voltage of 45 V, the actuator reached a maximum velocity of 13 rad/s. This speed is mainly limited by the supply voltage. This was validated by testing the maximum speed at a range of supply voltages. The motor controller has a maximum input of 46 V, however the actual input voltage must be kept below this. Regenerative braking and noise can cause voltage spikes that trigger over-voltage faults. Therefore, in actual applications like the pendulum test, the voltage must be reduced more, limiting the speed further.

2) Maximum Torque: For the maximum torque test, the same torque ramp script is used. A quicker ramp, up to a higher peak was configured. The test was repeated with increasing torque peaks until failure occurred.

At torques above 70 Nm, the reducer started to get stuck. requiring an opposite torque to brake loose again. After a test of up to 80 Nm, disassembly was required. This showed that the onyx disk had deformed slightly, making it fit tighter within the pinwheel. Around the output pins was a noticeable increase in play.

The deformed disk was replaced with one printed in PC-CF. This is more rigid but less wear-resistant. The Onyx pinwheel was left in place as it showed no defects yet. With this configuration, torques up to 100 Nm were achieved. At this last test, the disk got stuck and required disassembly again. This time the pinwheel was visibly deformed with flattened lobes. The PC-CF disk showed no noticeable deformations, other than slightly increased play around the output pins.

None of the structural parts showed any deformations or fractures. This suggests that the limiting factor of the current prototypes, is the material of the reducer parts. Specifically, contact stiffness and yield strength appear to be the primary constraints.

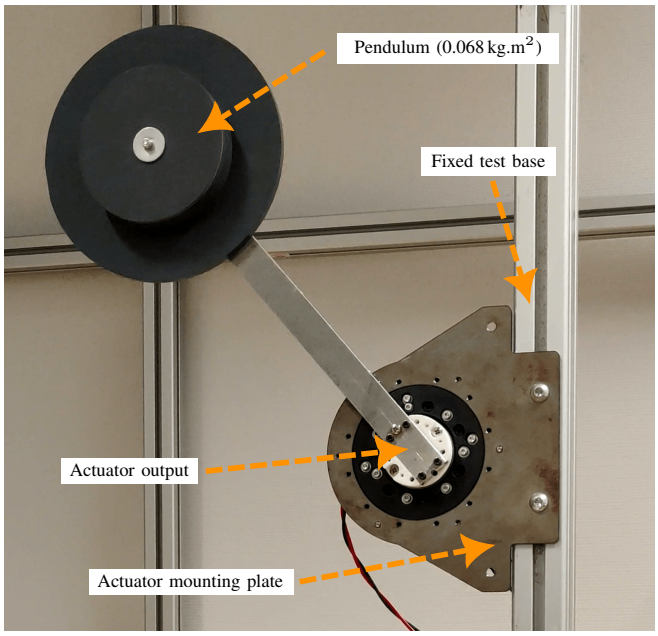

Fig. 19: Mounted actuator with pendulum.

3) Dynamic performance: The intended application of this actuator is legged robots. These encounter highly dynamic loads. The performance of the actuator in such an application was tested using a pendulum. The actuator is commanded to move between several points with limited speed and acceleration. The motor controller creates a smooth trajectory based on these limits. The movements are repeated at increasing acceleration limits.

The pendulum consists of a solid aluminum bar with plastic disks mounted at a radius of 30 cm. The bar has a mass of 0.23 kg, and the disks a total of 0.68 kg. This results in a combined inertia of 0.068 kg.m^2. The test setup with the mounted actuator and pendulum can be seen in Fig. 19.

The motor controller uses a combination of regenerative braking and flux braking. The power sinking capabilities of the used power supply were limited, which resulted in an over-voltage of the motor controller supply. To avoid this, the tests needed to be run at a reduced supply voltage of 32V. At this voltage, the maximum achievable velocity was around 9 rad/s. This velocity was set as a limit for the trajectory

generation. The maximum acceleration used was 100 rad/s^2. Higher accelerations were tested but again resulted in over-voltage faults, even at the reduced supply voltage.

Data is collected throughout the motions. Results are shown in Fig. 20. The trajectory tracking performance appears good, especially at lower accelerations such as detailed in Fig. 21a. The speed limit becomes evident when the velocity drops below the control velocity. At these moments, the control torque increases until it reaches a configured limit, in this case 100 Nm. At higher accelerations, a noticeable delay becomes apparent between the control position and the actual position. A close-up of this is shown in Fig. 21b. Part of this is because the motor controller advances to the next point as soon as the control position matches the command position, ignoring the true position. This can also be improved further by optimizing the tuning of the positional PID controller.

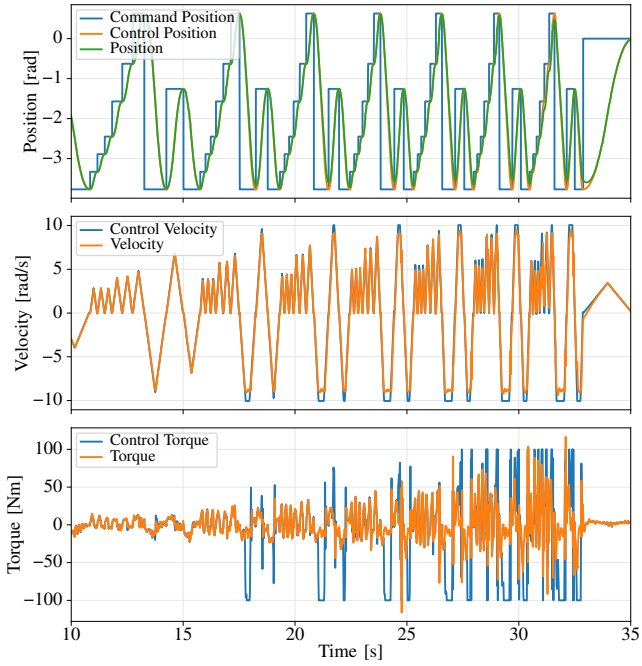

Fig. 20: Partial view of the trajectory following test.

During these higher accelerations, torque spikes exceeding 100 Nm were observed. This surpassed the torques from the maximum torque tests but did not cause any failures.

V. Discussion

The results of the anti-backlash mechanism tests, mainly those in Fig. 14, show a clear decrease in play for both anti-backlash mechanisms as preload is increased. The resulting play is significantly smaller than that of the baseline model. After the initial run-in, an increase in play is noticeable. All designs began with a clearance allowance to improve the ease of assembly and to ensure the anti-backlash mechanism could operate effectively. This play in the baseline model meant lower friction and minimal wear during run-in. The split pinwheel was designed with clearances equal to the baseline.

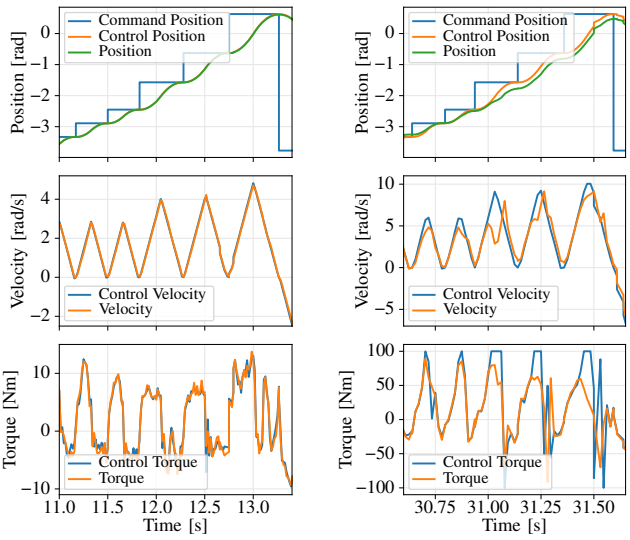

(a) Low accelerations (19 rad/^{2}). (b) High accelerations (100 rad/^{2}).

Fig. 21: Close-ups of the trajectory following data.

The initial play is lower, which may be due to a slight initial preload or manufacturing variability. After the run-in, both perform nearly identical. The conic disk design started with a fairly tight fit after which the run-in shows a significant impact on play and friction. The layer lines of the 3D-printed components are expected to wear down first. We suspect this to have the largest impact on the conic disk mechanism due to its sloped edges. During printing, these are approximated as a stepped pattern. The same is true for the sloped segments of the split-pinwheel design. However, these parts experience less motion and will therefore not wear down as quickly.

As preload is increased, a decrease in play and an increase in friction is noticeable. Some play does remain at maximal preload. We suspect this comes from clearance around the output pins and hysteresis of the reducer materials. The optimal preload setting depends on the application, balancing the trade-off between minimal play and reducing friction. The split-pinwheel design seems to perform better overall based on this trade-off, as shown in the Pareto front of Fig. 18. When minimizing play is less critical, the baseline design may be preferable due to its lower friction. However, this does not account for the stiffness of the reducer. In the conic design, stiffness appears to be largely unaffected by increased preload. In contrast, the split pinwheel design shows a reduction in estimated stiffness as preload increases. This effect is counterintuitive as a higher preload is expected to result in a stiffening effect.

Issues with speed and high accelerations were primarily due to reverse power spikes that led to an unstable supply voltage. This meant the requirement of 130 RPM could not be reached. This also caused limitations in the trajectory following tests. Torque was only limited by the material stiffness and yield strength of the reducer parts. None of

the structural components showed any failures, making it worthwhile to further optimize the materials, print settings, and design of the cycloidal disk and non-pinwheel. Furthermore, the torque and stiffness tests were done in a static situation with a locked output. During dynamic loads, the effects may be different. This is already seen during the pendulum test that shows torque peaks exceeding 100 Nm without failure. These results suggest that a lower reduction ratio might be better suited for the current design, increasing speed and limiting the maximum torque to a level more compatible with the reduction stage's capabilities.

VI. Conclusions and Future Work

This paper proposes two novel anti-backlash mechanisms. One is based on a conically shaped cycloidal disk, and another is based on a split non-pinwheel part. Both mechanisms were shown to be effective in an experimental comparison with a baseline design. Adjustable preload within the mechanisms reduces play at the cost of increased friction. This is a trade-off that can be made based on the intended application.

These experimental results prove the feasibility of anti-backlash mechanisms for cycloidal drives. However, more research is required to fully understand the implications of such a mechanism. As can be seen in Fig. 8, the meshing with an undersized disk differs from the ideal multi-tooth contact of non-pinwheel cycloidal drives. We suspect this is part of the reason for the decrease in reducer stiffness. The different meshing patterns may also have other optimal design parameters. The impact of non-uniform manufacturing errors must also be studied further.

The mechanisms were integrated into a compact design with performance competitive with state-of-the-art QDD designs from recent literature. It is cost-effective due to the use of 3D-printed components. Torques exceeding 100 Nm were tested, but sustained torques above 70 Nm resulted in plastic deformation of the cycloidal disk and non-pinwheel part. The main limitation is the yield strength and contact stiffness of the material for the reducer parts. Several improvements are still possible with these parts that are worth testing, such as optimized print settings, design tweaks, and alternative materials.

Further design optimizations are possible, such as increasing certain clearances and better accounting for the quality of support surfaces. Also, the alignment of parts during assembly can use improvements. Furthermore, the current design is such that all three configurations are implemented into a single solution with minimal modifications. When only one of the anti-backlash mechanisms is selected, the design can be simplified and optimized further. Active cooling of the actuator is also suggested. Continuous motion at higher speeds, such as during run-in, resulted in temperatures up to 55 °C at the motor windings. This can have a significant impact on the stiffness of the 3D-printed components, as was experienced with one of the tested alternative materials.

The use of 3D-printed components allows for low-cost, customizable designs, but the lower tolerance can introduce additional play. Anti-backlash mechanisms offer a practical solution to this issue, improving performance without significantly increasing cost. This makes them a viable approach to enhance the precision and reliability of 3D-printed parts, especially in applications where cost-effectiveness is critical.

References

[1] B. Katz, "A low cost modular actuator for dynamic robots," 2018. [Online]. Available: https://www.semanticscholar.org/paper/A-low-cost-modular-actuator-for-dynamic-robots-Katz/80732f8a46655aa4a1037a7fbdc154f4ceb33c50 (visited on 02/11/2024).

[2] T. Zhu, "Design of a Highly Dynamic Humanoid Robot," en, Ph.D. dissertation, 2023. [Online]. Available: https://escholarship.org/uc/item/0qz3p57g.

[3] W. Roozing and G. Roozing, "Experimental comparison of pinwheel and non-pinwheel designs of 3D-printed cycloidal gearing for robotics," en, 2024.

[4] W. Roozing and G. Roozing, "3D-printable low-reduction cycloidal gearing for robotics," en, in *2022 IEEE/RSJ International Conference on Intelligent Robots and Systems (IROS)*, Kyoto, Japan: IEEE, Oct. 2022, pp. 1929–1935, ISBN: 978-1-66547-927-1. DOI: 10.1109/IROS47612.2022.9982006. [Online]. Available: https://ieeexplore.ieee.org/document/9982006/ (visited on 01/24/2024).

[5] K. Lee, S. Hong, and J.-H. Oh, "Development of a Lightweight and High-efficiency Compact Cycloidal Reducer for Legged Robots," en, *International Journal of Precision Engineering and Manufacturing*, vol. 21, no. 3, pp. 415–425, Mar. 2020, ISSN: 2005-4602. DOI: 10.1007/s12541-019-00215-9. [Online]. Available: https://doi.org/10.1007/s12541-019-00215-9 (visited on 01/29/2024).

[6] A. Singh, N. Kashiri, and N. Tsagarakis, "Design of a Quasi-Direct-Drive Actuator for Dynamic Motions," en, *Proceedings*, vol. 64, no. 1, p. 11, 2020, Number: 1 Publisher: Multidisciplinary Digital Publishing Institute, ISSN: 2504-3900. DOI: 10.3390/IeCAT2020-08516. [Online]. Available: https://www.mdpi.com/2504-3900/64/1/11 (visited on 03/19/2024).

[7] C. A. Perez-Dıaz, I. Munoz, D. Martin-Hernandez, *et al.*, "Design and Experimental Characterisation of a Novel Quasi-Direct Drive Actuator for Highly Dynamic Robotic Applications," en, May 2024.

[8] S. Yu, T.-H. Huang, X. Yang, *et al.*, "Quasi-Direct Drive Actuation for a Lightweight Hip Exoskeleton With High Backdrivability and High Bandwidth," *IEEE/ASME Transactions on Mechatronics*, vol. 25, no. 4, pp. 1794–1802, Aug. 2020, Conference Name: IEEE/ASME Transactions on Mechatronics, ISSN: 1941-014X. DOI: 10.1109/TMECH.2020.2995134. [Online]. Available: https://ieeexplore.ieee.org/document/9095261 (visited on 03/21/2024).

[9] W. Luo, G. Liu, and H. Wang, "Study on Anti-backlash Mechanism Used in Precise Transmission: A Review," en, in *Advances in Mechanical Design*, J. Tan, Ed., ser. Mechanisms and Machine Science, Singapore: Springer Nature, 2022, pp. 1449–1470, ISBN: 9789811673818. DOI: 10.1007/978-981-16-7381-8_89.

[10] *GO-M8010-6 Motor*, en. [Online]. Available: https://shop.unitree.com/products/go1-motor (visited on 03/21/2024).

[11] *Unitree H1*, en. [Online]. Available: https://shop.unitree.com/products/unitree-h1 (visited on 03/21/2024).

[12] Y. Kariyama and K. Zushi, "Relationships between lower-limb joint kinetic parameters of sprint running and rebound jump during the support phases," *The Journal of Physical Fitness and Sports Medicine*, vol. 5, pp. 187–193, May 2016. DOI: 10.7600/jpfsm.5.187.

[13] K. Embry, *The Effect of Walking Incline and Speed on Human Leg Kinematics, Kinetics, and EMG*, en, Oct. 2018. [Online]. Available: https://ieee-dataport.org/open-access/effect-walking-incline-and-speed-human-leg-kinematics-kinetics-and-emg (visited on 03/21/2024).

[14] Z. Yang, J. Shang, Z. Luo, X. Wang, and N. Yu, "Nonlinear Dynamics Modeling and Analysis of Torsional Spring-Loaded Antibacklash Gear with Time-Varying Meshing Stiffness and Friction," en, *Advances in Mechanical Engineering*, vol. 5, p. 203 438, Jan. 2013, Publisher: SAGE Publications, ISSN: 1687-8132. DOI: 10.1155/2013/203438. [Online]. Available: https://doi.org/10.1155/2013/203438 (visited on 01/31/2024).

[15] J. Zhang, B. Chen, Q. Zhang, J. Koo, and S. Lyu, "New Type of Cycloid Planetary Reducer for Precision Transmission," en, 2009.

[16] bsmith2123, *The 4130 Movement in the Rolex Daytona has spring loaded gears to prevent backlash - incredible innovation at such scale*, Reddit Post, Nov. 2021. [Online]. Available: www.reddit.com/r/EngineeringPorn/comments/qmtsj8/the_4130_movement_in_the_rolex_daytona_has_spring/ (visited on 03/16/2024).

[17] Q. Du, T. Zhang, G. Yang, C.-Y. Chen, W. Wang, and C. Zhang, "A 3K Planetary Gear Train with a flexure-based anti-backlash carrier for collaborative robots," en, *Mechanism and Machine Theory*, vol. 191, p. 105 495, Jan. 2024, ISSN: 0094114X. DOI: 10.1016/j.mechmachtheory.2023.105495. [Online]. Available: https://linkinghub.elsevier.com/retrieve/pii/S0094114X23002665 (visited on 01/25/2024).

[18] J. Sensinger, "Unified Approach to Cycloid Drive Profile, Stress, and Efficiency Optimization," *Journal of Mechanical Design - J MECH DESIGN*, vol. 132, Feb. 2010. DOI: 10.1115/1.4000832.

[19] J. W. Sensinger, "Efficiency of High-Sensitivity Gear Trains, Such as Cycloid Drives," en, *Journal of Mechanical Design*, vol. 135, no. 7, p. 071 006, Jul. 2013, ISSN: 1050-0472, 1528-9001. DOI: 10.1115/1.4024370. [Online]. Available: https://asmedigitalcollection.asme.org/mechanicaldesign/article/doi/10.1115/1.4024370/375635/Efficiency-of-HighSensitivity-Gear-Trains-Such-as (visited on 01/24/2024).

[20] C.-F. Hsieh, "Dynamics Analysis of Cycloidal Speed Reducers With Pinwheel and Nonpinwheel Designs," en, *Journal of Mechanical Design*, vol. 136, no. 9, p. 091 008, Sep. 2014, ISSN: 1050-0472, 1528-9001. DOI: 10.1115/1.4027850. [Online]. Available: https://asmedigitalcollection.asme.org/mechanicaldesign/article/doi/10.1115/1.4027850/376079/Dynamics-Analysis-of-Cycloidal-Speed-Reducers-With (visited on 01/24/2024).

[21] S. Pabiszczak and M. Kowal, "Efficiency of the eccentric rolling transmission," en, *Mechanism and Machine Theory*, vol. 169, p. 104 655, Mar. 2022, ISSN: 0094114X. DOI: 10.1016/j.mechmachtheory.2021.104655. [Online]. Available: https://linkinghub.elsevier.com/retrieve/pii/S0094114X21003852 (visited on 01/24/2024).

[22] J. W. Sensinger and J. H. Lipsey, "Cycloid vs. harmonic drives for use in high ratio, single stage robotic transmissions," *2012 IEEE International Conference on Robotics and Automation*, pp. 4130–4135, May 2012, Conference Name: 2012 IEEE International Conference on Robotics and Automation (ICRA) ISBN: 9781467314053 9781467314039 9781467315784 9781467314046 Place: St Paul, MN, USA Publisher: IEEE. DOI: 10.1109/ICRA.2012.6224739. [Online]. Available: http://ieeexplore.ieee.org/document/6224739/ (visited on 09/02/2024).

[23] M. Nordin and P.-O. Gutman, "Controlling mechanical systems with backlash—a survey," en, *Automatica*, vol. 38, no. 10, pp. 1633–1649, Oct. 2002, ISSN: 00051098. DOI: 10.1016/S0005-1098(02)00047-X. [Online]. Available: https://linkinghub.elsevier.com/retrieve/pii/S000510980200047X (visited on 02/02/2024).

[24] P. M. Allan and N. M. Levy, "The Determination of Minimum Pre-Load Torque for Antibacklash Gears in a Positional Servomechanism," *IEEE Transactions on Industrial Electronics and Control Instrumentation*, vol. IECI-27, no. 1, pp. 26–29, Feb. 1980, Conference Name: IEEE Transactions on Industrial Electronics and Control Instrumentation, ISSN: 2375-0502. DOI: 10.1109/TIECI.1980.351657. [Online]. Available: https://ieeexplore.ieee.org/abstract/document/4159493 (visited on 02/01/2024).

[25] P. Gould, *Anti-Backlash 3D Printed Cycloidal BLDC Actuator*, en, May 2019. [Online]. Available: https://hackaday.io/project/165592-anti-backlash-3d-printed-cycloidal-bldc-actuator (visited on 07/30/2024).

[26] Z. Cui, C. Song, F. Zhu, and C. Zhu, "Research on Tolerance Design of 2K-V Reducer with Beveloid Gear Considering the Effect of Anti-Backlash," en, *International Journal of Precision Engineering and Manufacturing*, Nov. 2023, ISSN: 2005-4602. DOI: 10.1007/

s12541-023-00916-2. [Online]. Available: https://doi.org/10.1007/s12541-023-00916-2 (visited on 01/25/2024).

[27] K.-F. Scheufele, "Toothed gear with backlash compensation, in particular for timepieces," en, EP2003522A1, Dec. 2008. [Online]. Available: https://patents.google.com/patent/EP2003522A1/en (visited on 03/14/2024).

[28] S. Bannier, N. Bonvin, and D. Passannante, "Gear with backlash compensation for a timepiece mechanism," en, EP2112567A1, Oct. 2009. [Online]. Available: https://patents.google.com/patent/EP2112567A1/en (visited on 03/14/2024).

[29] J. Volbeda, *MSc Thesis - Cost-Effective and Torque-Dense Cycloidal Actuator with Anti-Backlash Mechanisms*, en, Sep. 2024. [Online]. Available: https://github.com/JelmerV/Anti-Backlash-Cycloidal-Actuator (visited on 09/03/2024).

[30] T. Lenzi, J. Lipsey, and J. W. Sensinger, "The RIC Arm—A Small Anthropomorphic Transhumeral Prosthesis," *IEEE/ASME Transactions on Mechatronics*, vol. 21, no. 6, pp. 2660–2671, Dec. 2016, Conference Name: IEEE/ASME Transactions on Mechatronics, ISSN: 1941-014X. DOI: 10.1109/TMECH.2016.2596104. [Online]. Available: https://ieeexplore.ieee.org/document/7539396 (visited on 01/29/2024).

[31] T. Li, X. An, X. Deng, J. Li, and Y. Li, "A New Tooth Profile Modification Method of Cycloidal Gears in Precision Reducers for Robots," en, *Applied Sciences*, vol. 10, no. 4, p. 1266, Jan. 2020, Number: 4 Publisher: Multidisciplinary Digital Publishing Institute, ISSN: 2076-3417. DOI: 10.3390/app10041266. [Online]. Available: https://www.mdpi.com/2076-3417/10/4/1266 (visited on 02/05/2024).

[32] mjbots, *Fdcanusb*, en. [Online]. Available: https://mjbots.com/products/fdcanusb (visited on 08/03/2024).